Chemical Science

ROYAL SOCIETY OF CHEMISTRY

EDGE ARTICLE

View Article Online
View Journal

Cite this: DOI: 10.1039/d6sc00386a

All publication charges for this article have been paid for by the Royal Society of Chemistry

Mixed-valence Ru nanoparticles anchored on N-rich metal-phthalocyanine/graphene vdW heterostructures for hydrogen-bond-assisted alkaline hydrogen evolution

Zichong Xiang,†[a] Guanping Wei,†[a] Aifeng Yang,[a] Shangyu Li,[a] Sitian Xu,[a] Yuelong Zhou,[a] Longbin Li*[ab] and Yiwang Chen *[abc]

Hydrogen production *via* alkaline anion-exchange membrane H_2O electrolysis (AEMWE) is constrained by sluggish hydrogen evolution reaction (HER) kinetics associated with H_2O dissociation and hydroxyl management. Here, we report a pyrolysis-free Ru nanoparticles anchored on a two-dimensional metal-phthalocyanine/graphene vdW heterostructure (Ru@NiFe PPc) electrocatalyst for alkaline HER. The N-rich macrocyclic phthalocyanine framework and strong Ru-N coordination enable the uniform and stable dispersion of the mixed-valence Ru nanoparticles. The high-valence Ru centers accelerate interfacial H_2O dissociation and hydroxyl transfer, whereas the Ru^0 sites facilitate *H desorption. Thus, Ru@NiFe PPc delivers exceptional HER performance with only 15 mV at 10 mA cm^{-2}, surpassing the best-performing Ru-based catalysts. As an AEMWE cathode, Ru@NiFe PPc delivers an industrial-scale current density of 2.0 A cm^{-2} at 2.09 V. In a hybrid electrolyzer coupling HER with low-potential 5-hydroxymethylfurfural oxidation, the system delivers 100 mA cm^{-2} at an ultralow cell voltage of 0.30 V. Theory calculations reveal that hydrogen-bond-assisted H_2O adsorption on Ru nanoparticles, and the electronic coupling between Ru nanoparticles and phthalocyanine matrix weakens *OH binding, effectively lowering the overall HER barrier. This work elucidates the full alkaline HER pathway involving all key intermediates and opens a new avenue for the design of pyrolysis-free Ru-based HER catalysts.

Received 14th January 2026
Accepted 26th March 2026

DOI: 10.1039/d6sc00386a

rsc.li/chemical-science

1 Introduction

Hydrogen (H_2), widely recognized as an ideal alternative to fossil fuels, plays a pivotal role in achieving global carbon neutrality and driving sustainable energy transitions.[1–5] Among the various H_2 production pathways, electrocatalytic H_2O splitting offers a clean and scalable strategy, yet its widespread implementation is hindered by prohibitive costs and substantial energy consumption.[6–11] Compared with acidic electrolysis, alkaline H_2O electrolysis features lower activation barriers for the anodic oxygen evolution reaction,[12–15] thereby reducing the overall energy input required for H_2 production. Additionally, the alkaline hydrogen evolution reaction (HER) mitigates catalyst corrosion and dissolution, making it particularly attractive for practical applications.[16] Recently, anion-exchange membrane H_2O electrolysis (AEMWE) has garnered increasing attention in industrial H_2 production due to its fast start-up/shut-down capability, compatibility with fluctuating renewable energy, and use of fluorine-free membranes and cost-effective stack hardware.[6,7] However, the commercial deployment of AEMWE is substantially restricted by the sluggish cathodic alkaline HER kinetics, which are approximately 2–3 orders of magnitude slower than those in acidic environments.[17–19] The alkaline HER involves several fundamental steps, including H_2O dissociation (Volmer step), hydroxide (OH^-) transfer, followed by the Heyrovsky or Tafel pathways to generate H_2. Consequently, the dissociative adsorption energy of H_2O and the adsorption energies of active H (*H) and hydroxyl (*OH) intermediates constitute three key and interrelated parameters that dictate alkaline HER performance.[20] At present, noble-metal catalysts such as Pt and Ir represent state-of-the-art benchmarks for alkaline HER owing to their optimal *H adsorption energetics.[21,22] However, their high cost, limited durability, and low atomic utilization efficiency further impede practical application. Notably, the market price of Ru amounts to merely one quarter of that of Pt and approximately one sixth of that of Ir, and Ru-based electrocatalysts exhibit comparable or even superior alkaline HER activity relative to Pt. Therefore,

[a]College of Chemistry and Materials, Gannan Normal University, Ganzhou 341000, China. E-mail: longbin-li@gnnu.edu.cn; ywchen@gnnu.edu.cn

[b]Centre for Advanced Optoelectronics, School of Intelligent Manufacturing and Future Energy, Gannan Normal University, Ganzhou 341000, China

[c]College of Chemistry and Chemical Engineering, Film Energy Chemistry for Jiangxi Provincial Key Laboratory (FEC), Institute of Polymers and Energy Chemistry (IPEC), Nanchang University, Nanchang 330031, China

† These authors contributed equally to this work.

exploring cost-effective Ru-based electrocatalysts holds substantial importance for advancing the efficiency of alkaline HER.[23–26]

Recently, conjugated microporous polymer-based materials with tunable electronic structures and ordered network frameworks have emerged as a versatile platform for electrocatalysis.[27–29] Among them, owing to the fully π-conjugated macrocycles, N-rich coordination environment, and robust metal-binding capability, metal phthalocyanines and their polymeric derivatives display appreciable catalytic activity for H_2O-splitting processes.[30,31] Although many studies reveal that electrodeposition enables the anchoring of single-atom Ru sites onto N-rich scaffolds, thereby constructing highly active catalytic interfaces for alkaline HER. However, a single Ru component is insufficient to simultaneously satisfy the requirements for efficient alkaline HER. Typically, high-valence Ru species promote interfacial H_2O dissociation, whereas metallic Ru^0 sites play a complementary role by facilitating *H desorption, thereby collectively accelerating the HER.[32–34] Moreover, metal phthalocyanines were found as a universal "atom-glue" to stabilize the Pt-based intermetallic nanoparticles, thereby achieving markedly enhanced electrocatalysis activity and durability. For instance, Huang *et al.* developed a universal "atom-glue" strategy, in which metal–nitrogen–carbon (M–N–C)-derived Pt-M-N coordination forms a stabilizing interfacial glue that prevents sintering of Pt-based intermetallics, thereby achieving markedly enhanced electrocatalytic activity and durability.[35] Therefore, precisely controlling the distribution of Ru species with different valence states on metal phthalocyanines or their polymeric derivatives represents a viable strategy for constructing highly active and durable catalysts for alkaline HER.[36]

In this work, we constructed a Ru nanoparticles anchored on a two-dimensional (2D) metal phthalocyanine/graphene vdW heterostructure (Ru@NiFe PPc) catalyst through pyrolysis-free mechanical ball-milling and electrochemical deposition strategies. The N-rich architecture of the metal phthalocyanine polymer establishes robust interfacial interactions with the Ru nanoparticles, promoting homogeneous dispersion and reinforcing the stability of the Ru nanostructures. Meanwhile, the coexisting Ru^{4+} and Ru^0 sites respectively function as the active centers for H_2O dissociation and *H desorption during the hydrolysis process. In addition, the constructed 2D metal phthalocyanine/graphene vdW heterostructure not only enhances the site utilization, optimizes the mass transport, and improves the conductivity, which endows Ru@NiFe PPc with excellent electrocatalytic HER activity and fast kinetics. Benefiting from these synergistic effects, the Ru@NiFe PPc catalyst exhibits outstanding HER performance, requiring only 15 mV of overpotential to reach 10 mA cm^{-2} and delivering a low Tafel slope of 39 mV dec^{-1}, surpassing commercial Pt/C and most reported catalysts. Furthermore, an AEMWE assembled with Ru@NiFe PPc cathode and commercial $NiFeO_x$ anode achieves a current density of 2.0 A cm^{-2} at a low cell voltage of 2.09 V. More importantly, a dual-electrode H_2 production system is demonstrated, wherein low-potential aldehyde oxidation is coupled with HER at both electrodes, enabling bipolar H_2 generation below 0.1 V and delivering 100 mA cm^{-2} at only 0.30 V. Density functional theory (DFT) calculations indicate that the N sites on the phthalocyanine framework polarize the H_2O molecule adsorbed on the Ru nanoparticles through a H-bonding interaction, leading to a pronounced elongation of the O–H bond and facilitating H_2O dissociation. Furthermore, the strong interaction between the phthalocyanine polymer and the Ru nanoparticles promotes *H desorption and weakens *OH adsorption, thereby lowering the overall energy barrier for the alkaline HER. This work establishes a scalable synthesis of highly active Ru-based alkaline HER electrocatalysts while providing a model platform to elucidate the mechanistic intricacies of H_2O splitting toward sustainable H_2 production.

2 Results and discussion

2.1 Synthesis and characterization of the Ru@NiFe PPc

The Ru@NiFe PPc was successfully prepared through a combination of solvothermal and electrochemical deposition methods as shown in Fig. 1a. Firstly, a series of precursor compounds, including iron(II) tetranitrophthalocyanine (FeTNPc), nickel(II) tetranitrophthalocyanine (NiTNPc), and nickel(II) tetraaminophthalocyanine (NiTAPc) were synthesized *via* a solvothermal process. Precursor morphology was characterized by scanning electron microscopy (SEM; Fig. S1 and Table S1). The UV-Vis spectra of FeTNPc, NiTNPc, NiTAPc, and iron(II) phthalocyanine (FePc) display the characteristic Q-band (600–800 nm) and B-band (300–400 nm) absorptions, confirming the formation of the metal phthalocyanine structure (Fig. S2).[27] Fourier-transform infrared (FT-IR) spectroscopy further verifies formation of the phthalocyanine framework through its diagnostic vibrations (Fig. S3).[37,38] Subsequently, the Ni, Fe phthalocyanine-based polymer network (NiFe PPc) was constructed through a polymerization reaction. SEM images (Fig. S4) and Transmission electron microscopy (TEM) images (Fig. S5) reveal that NiFe PPc adopts a 2D nanosheet morphology, the corresponding elemental composition determined by the energy-dispersive X-ray spectroscopy (EDS) of TEM was summarized in Table S2. The UV-vis and FTIR spectra of NiFe PPc confirm retention of the characteristic metal phthalocyanine framework (Fig. S6).

Then, the 2D NiFe PPc/graphene vdW heterostructure material (NiFe PPc@G) was prepared by direct ball-milling of NiFe PPc with graphene. Finally, Ru nanoparticles anchored on a 2D metal phthalocyanine/graphene vdW heterostructure (Ru@NiFe PPc) catalyst was obtained by cyclic voltammetry (CV) in a standard three-electrode cell containing Ar-saturated 0.5 M H_2SO_4 solution containing NH_4RuCl_6 (Fig. S7). As the deposition progressed, the electrolyte color gradually changed from brownish-yellow to pale yellow, indicating the continuous reduction and incorporation of Ru species onto the carbon paper-supported working electrode (Fig. S8). This deposition procedure ultimately yielded Ru nanoparticles uniformly distributed on the NiFe PPc surface. To optimize HER performance, Ru@NiFe PPc catalysts were prepared by adjusting the number of CV deposition cycles. For comparison, Ru

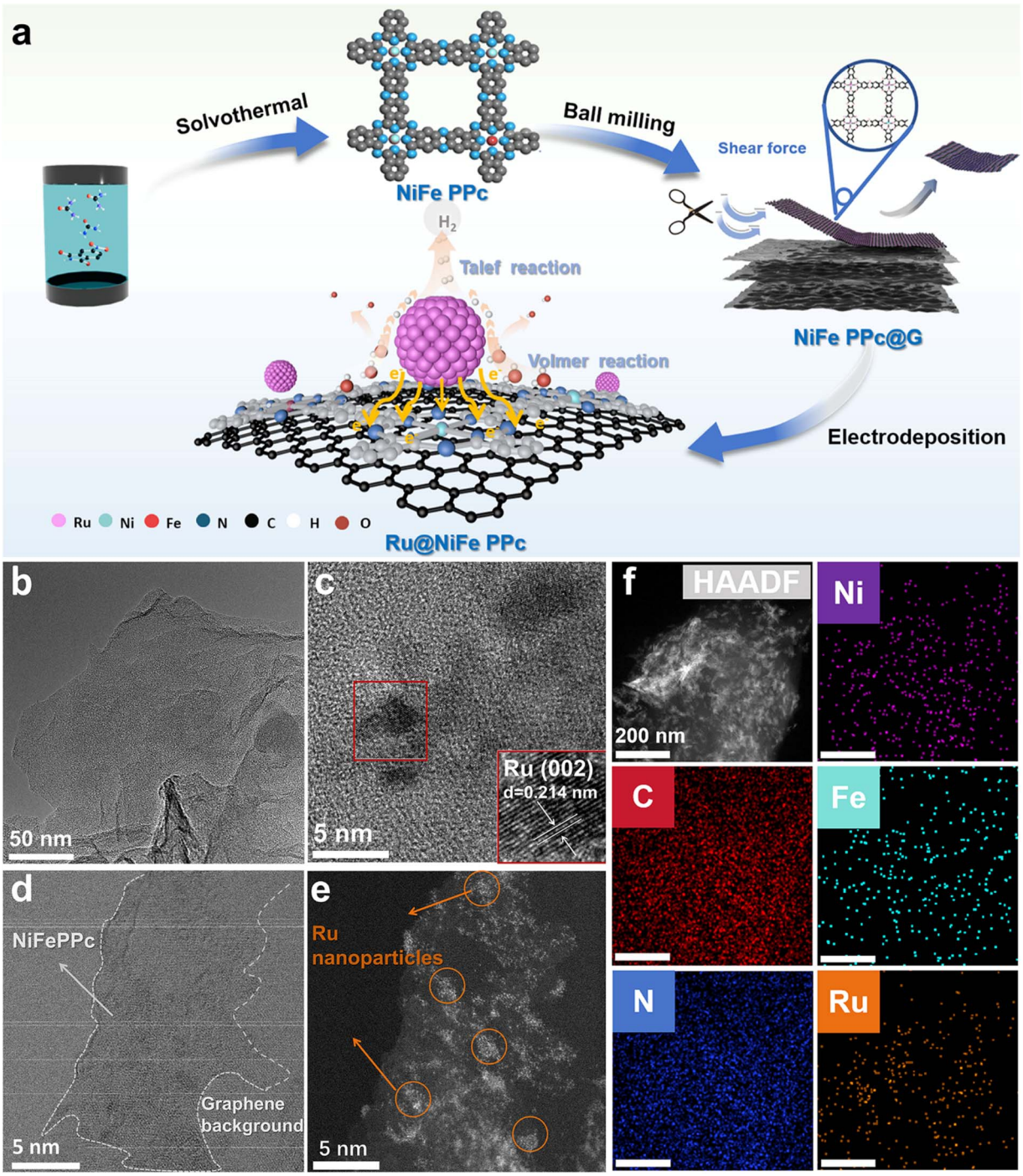

Fig. 1 Overview of the synthetic route and the subsequent structural and electron-microscopic characterizations. (a) Schematic illustrating the fabrication processes of Ru@NiFe PPc. (b) TEM image, (c) HRTEM image, (d–f) AC-STEM and HAADF-STEM images and EDX elemental mapping of Ru@NiFe PPc.

nanoparticles were directly electrodeposited onto pristine graphene (denoted Ru@G) using the same cyclic voltammetry protocol in the absence of the NiFe PPc framework. Synthetic details of the target preparation process are provided in the SI Experimental Section. TEM image confirms that Ru@NiFe PPc retains a well-defined nanosheet morphology (Fig. 1b and S9). High-resolution TEM (HRTEM) image revealed distinct lattice fringes with a *d*-spacing of 0.214 nm, indexed to the (002) plane of metallic Ru (Fig. 1c). Spherical aberration-corrected scanning TEM (AC-TEM) was further employed to elucidate the structural composition of Ru@NiFe PPc, wherein the NiFe PPc nanosheet matrix is clearly discerned from the underlying graphene support (Fig. 1d). The corresponding high-angle annular dark-field scanning TEM (HAADF-STEM) image reveals uniformly

distributed bright nanoparticles corresponding to metallic Ru, confirming preferential anchoring of Ru species onto 2D NiFe PPc/graphene heterostructure (Fig. 1e). The EDS mapping of Ru@NiFe PPc demonstrates homogeneous distribution of C, N, O, Fe, Ni, and Ru throughout the heterostructure (Fig. 1f), with the elemental compositions provided in Table S2. Furthermore, to substantiate the size-confinement effect imposed by the N-rich phthalocyanine framework on Ru crystallites, TEM characterization of Ru@G was performed for comparison. The results unambiguously demonstrate that the Ru nanoparticles on Ru@NiFe PPc exhibit markedly smaller grain sizes than those on Ru@G (Fig. S10). Fig. S11 presents the elemental mapping results of the Ru@G sample obtained from EDX analysis. This pronounced size suppression, arising from the confinement effect of the N-enriched phthalocyanine surface, facilitates a more homogeneous dispersion of Ru species and consequently increases the density of catalytically accessible active sites.

As shown in Fig. 2a, X-ray diffraction (XRD) patterns further confirm the structural composition of the catalysts. XRD pattern of Ru@NiFe PPc show a weaker and broader diffraction peak at ~44.0° compared to Ru@G, corresponding to the (002) plane of metallic Ru (JCPDS no. 06-0663).[25] This indicates substantial attenuation of Ru nanoparticles and reduced particle size, consistent with strong coordination and confinement of Ru nanoparticles by the N-rich NiFe PPc framework.[20] Notably, the predominant XRD diffraction peak arises from the carbon paper substrate. To evaluate the enhanced electrical conductivity imparted by graphene incorporation in the vdW heterostructure, ultrathin photoemission spectroscopy (UPS) measurements were performed on the catalysts. The calculated work functions of Ru@NiFe PPc, Ru@G, and NiFe PPc are 4.51, 4.72, and 4.96 eV, respectively, following the order NiFe PPc >

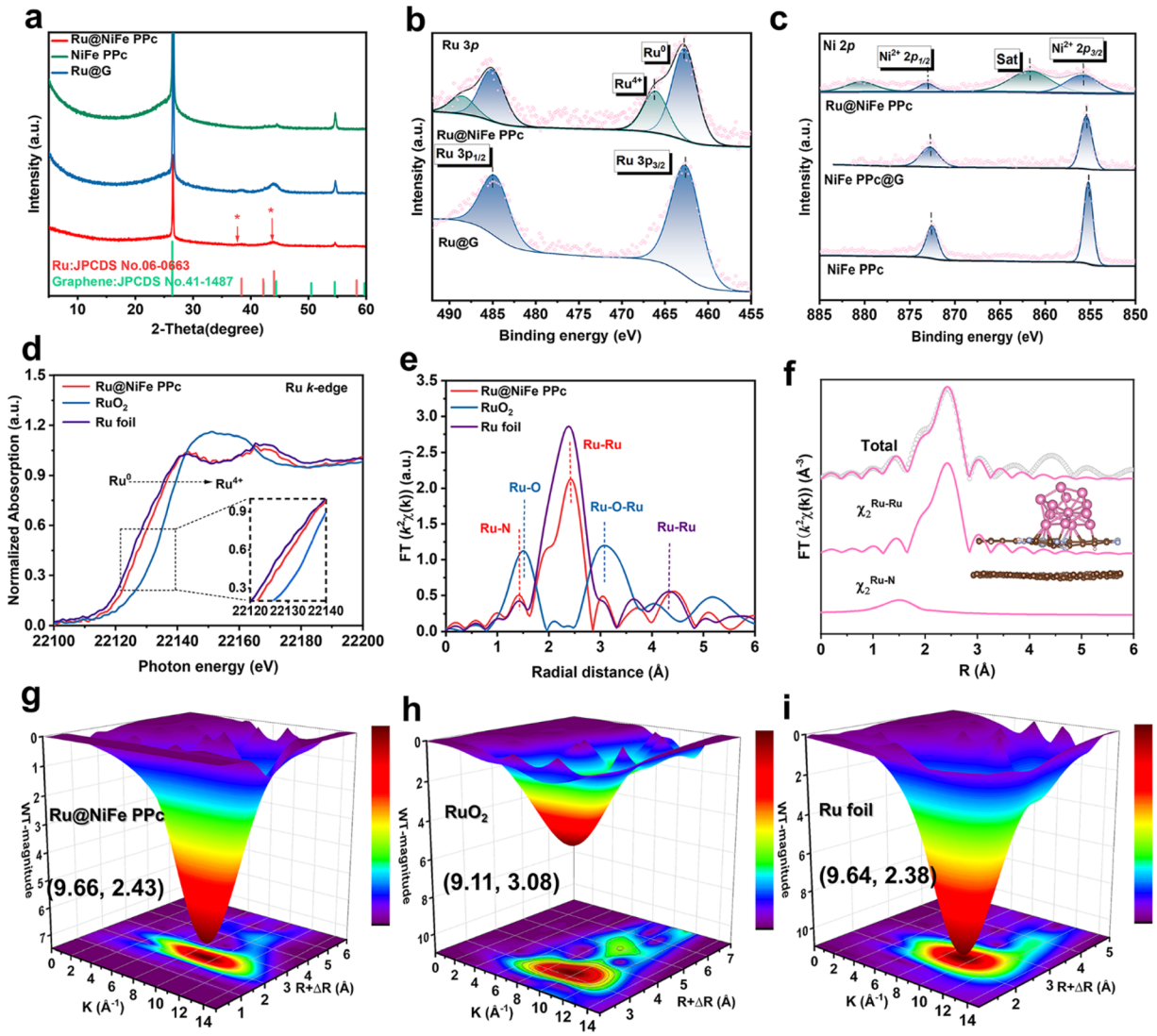

Fig. 2 Elemental composition and physicochemical characterization of the catalyst. (a) XRD patterns, (b) HR-XPS spectra of Ru 3p for Ru@NiFe PPc and Ru@G. (c) HR-XPS spectra of Ni 2p for Ru@NiFe PPc, NiFe PPc, and NiFe PPc@G. (d) XANES spectra at Ru K-edge, (e) the corresponding FT-EXAFS spectra, (f) the EXAFS analysis of Ru@NiFe PPc in *R* space, and (g–i) WT-EXAFS plots of Ru@NiFe PPc, RuO_2 and Ru foil.

Ru@G > Ru@NiFe PPc (Fig. S12). This trend suggests that constructing a vdW heterostructure between NiFe PPc and graphene enhances the electronic conductivity.[39]

The chemical composition and electronic states of materials were elucidated by X-ray photoelectron spectroscopy (XPS). The XPS survey spectrum of NiFe PPc (Fig. S13) confirms the presence of C, N, O, Fe, and Ni, whereas the survey spectrum of Ru@NiFe PPc (Fig. S14) exhibits an additional pronounced Ru signal, evidencing the successful incorporation of Ru species onto the 2D NiFe PPc/graphene heterostructure scaffold. The corresponding elemental compositions are summarized in Table S3. To precisely quantify the metal loadings, inductively coupled plasma-optical emission spectrometry analysis of Ru@NiFe PPc shows Ru, Fe, and Ni contents of 0.270, 0.015, and 0.049 wt%, respectively (Table S4), in close agreement with the targeted stoichiometry. The high-resolution XPS (HR-XPS) spectra clearly resolve the valence states of the metal centers and their electronic interactions with the coordinating ligands. The C 1s HR-XPS spectrum for Ru@NiFe PPc (Fig. S15) can be deconvoluted into three peaks converging on 284.0 eV (C═C), 284.8 (C–C), and 285.6 eV (C═N) for NiFe PPc/graphene scaffold. The Ru 3p HR-XPS spectra of Ru@NiFe PPc displays four peaks arising from spin–orbit splitting: the peaks at 462.73 and 485.06 eV are assigned to Ru^0 $3p_{1/2}$ and $3p_{3/2}$, while those at 466.09 and 488.50 eV correspond to Ru^{4+} species (Fig. 2b). In contrast, Ru@G exhibits only signals characteristic of metallic Ru0. This indicates that anchoring Ru nanoparticles onto the 2D NiFe PPc@G vdW heterostructure induces strong interfacial charge transfer, thereby rendering a fraction of the interfacial Ru species in the Ru^{4+} oxidation state.[40] Intriguingly, the high-resolution Ni 2p XPS spectrum of Ru@NiFe and PPc@G reveals Ni^{2+} $2p_{3/2}$ and Ni^{2+} $2p_{1/2}$ peaks at 855.89 and 873.14 eV, which positively shift by 0.45 and 0.35 eV relative to pristine NiFe PPc (Fig. 2c). Concomitantly, the N 1s HR-XPS spectra of Ru@NiFe PPc and NiFe PPc@G display two dominant peaks at 398.78 eV and 400.47 eV, assigned to C–N and metal–N bonds, which are also positively shifted compared to pristine NiFe PPc (Fig. S16). These observations indicate strong electronic interactions within the NiFe PPc/graphene vdW heterostructure, resulting in electron transfer from the NiFe PPc framework to the graphene layer.[39–42]

To further elucidate the local structure of Ru species, X-ray absorption near-edge structure (XANES) and extended X-ray absorption fine structure (EXAFS) measurements were performed using Ru foil and RuO_2 as reference standards. The Ru K-edge XANES of Ru@NiFe PPc lies between those of Ru foil and RuO_2, but is much closer to that of Ru foil, indicating that the majority of Ru species exist in the metallic Ru^0 state (Fig. 2d). The presence of a fraction of Ru^{4+} is attributed to strong interfacial interactions between the Ru nanoparticles and the N-rich NiFe PPc framework, consistent with partial electron transfer observed in XPS analysis. Fourier-transformed EXAFS spectra (Fig. 2e) reveal a Ru–N coordination shell at ~1.45 Å and Ru–Ru contribution at ~2.40 Å, confirming the direct coordination between Ru nanoparticles and the N atoms of the NiFe PPc framework.[43–46] In addition, the precise coordination configurations of Ru sites were further investigated by quantitative least-squares EXAFS curve-fitting analyses in both R and k spaces. The best-fitting analysis for Ru@NiFe PPc consists of Ru–Ru in the first shell and Ru–N in the second-shell (Fig. 2f and S17). The coordination number of N on Ru centres is 2 with an average bond distance of 2.01 Å, and the coordination number of Ru is 5.9 with a bond distance of 2.66 Å (Table S5). Wavelet transforms further resolve the two contributions with high clarity (Fig. 2g–i), unequivocally verifying direct Ru–N anchoring within the NiFe PPc scaffold. Collectively, these results confirm the successful preparation of Ru@NiFe PPc, featuring strongly anchored Ru nanoparticles on a 2D NiFe PPc/graphene vdW heterostructure, which enables the coexistence of mixed-valence Ru species for enhanced HER performance.[47]

2.2 Catalytic performance of Ru@NiFe PPc

With the robust anchoring environment and mixed-valence nature of Ru nanoparticles, the catalytic behaviors toward the alkaline HER were evaluated. The HER activity of the Ru@NiFe PPc catalysts was then assessed in N_2-saturated 1.0 M KOH under a conventional three-electrode setup. For comparison, NiFe PPc, Ru@G, and commercial 20 wt% Pt/C were tested under identical conditions. As shown in the linear sweep voltammetry (LSV) curves (Fig. 3a), Ru@NiFe PPc delivers the most impressive HER activity among all catalysts examined. It requires an overpotential as low as 15 mV to achieve 10 mA cm^{-2}, markedly outperforming NiFe PPc (265 mV), Ru@G (53 mV), and Pt/C (49 mV) (Fig. 3b). To determine the optimal catalytic composition, NiFe polyphthalocyanine with different Ni/Fe ratios was first synthesized and evaluated by LSV measurements. The results revealed that the NiFe polyphthalocyanine with a Ni : Fe ratio of 3 : 1 exhibited the best catalytic performance. Subsequently, Ru was electrochemically deposited using a series of controlled CV cycle numbers, enabling systematic screening and identification of the best-performing catalyst. (Fig. S18 and S19). To further elucidate the HER kinetics, Tafel slopes were extracted from the polarization curves (Fig. 3c). Ru@NiFe PPc exhibits a remarkably low Tafel slope of 39 mV dec^{-1}, substantially smaller than those of NiFe PPc (303 mV dec^{-1}), Ru@G (63 mV dec^{-1}), and Pt/C (48 mV dec^{-1}). Such a small slope indicates rapid kinetics following a Volmer–Tafel pathway, consistent with the accelerated H_2O dissociation and efficient H–H recombination enabled by the mixed-valence Ru^{4+}/Ru^0 ensemble.

To assess the intrinsic activity normalized to the electrochemically accessible surface area, the double-layer capacitance (C_{dl}) was extracted from CV curves obtained at varying scan rates under non-faradaic region. (Fig. S20). Ru@NiFe PPc delivers the highest C_{dl} (18.64 mF cm^{-2}) (Fig. 3d), indicating the largest electrochemically active surface area (ECSA) among all catalysts. The calculated ECSA values (Fig. S21 and Table S6) corroborate this trend, reflecting the combined contribution of the 2D conductive heterostructure and uniformly dispersed Ru nanoparticles in exposing abundant active sites.

Electrochemical impedance spectroscopy (EIS) was further employed to probe the interfacial charge-transfer resistance (R_{ct}). The Nyquist plots, together with the corresponding

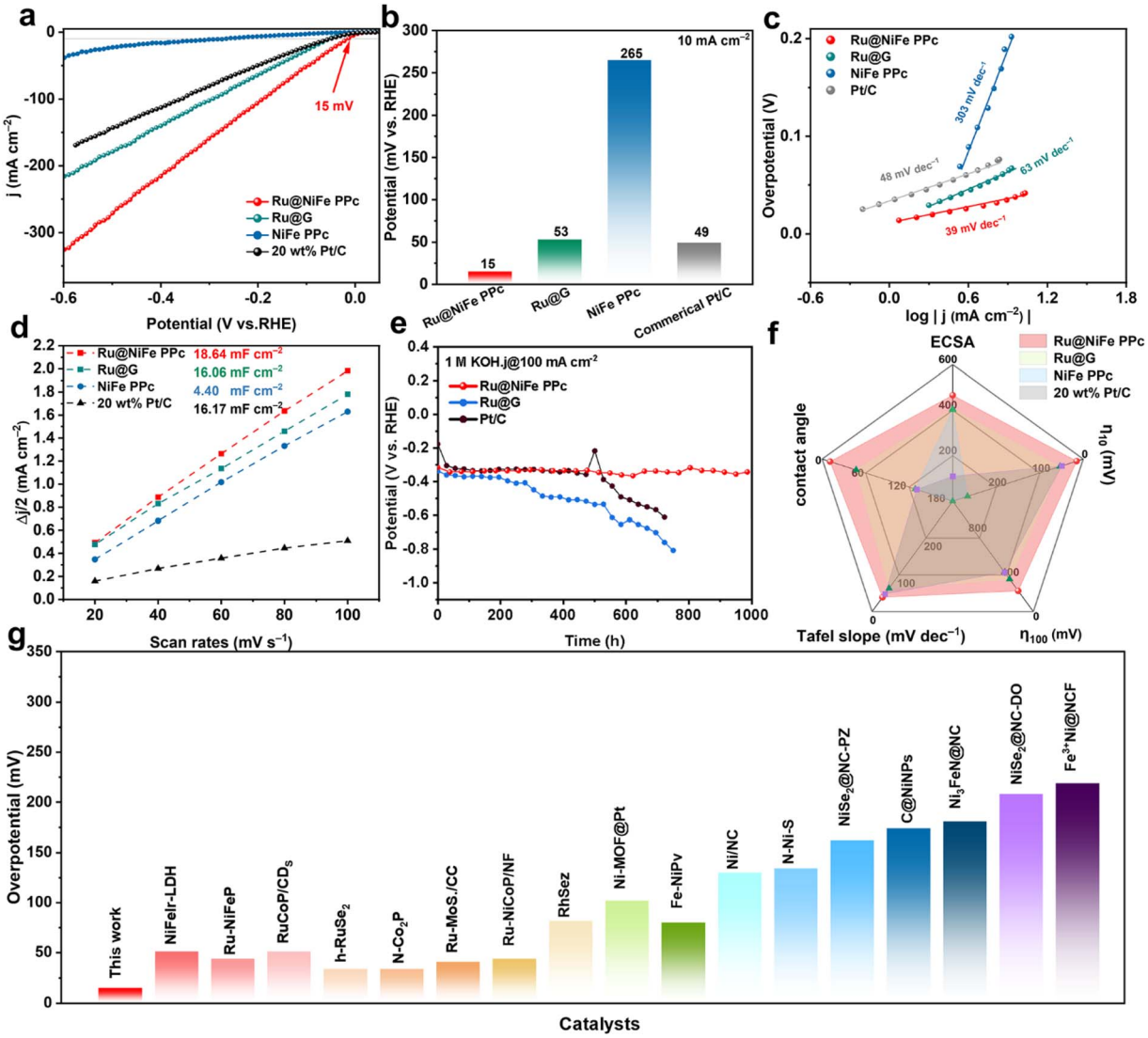

Fig. 3 Electrochemical performance of Ru@NiFe PPc, NiFe PPc, Ru@G, and 20 wt% commercial Pt/C in 1 M KOH. (a) HER polarization curves and (b) overpotentials at 10 mA cm^{-2}. (c) Tafel plots, (d) estimation of C_{dl} by plotting the current density variation. (e) Stable operation of the Ru@NiFe PPc, Ru@G and Pt/C running at −100 mV over 1000 h. (f) Comparison for the HER performance metrics of overpotential, Tafel slope, contact angle, and ECSA. (g) Comparison of overpotentials at 10 mA cm^{-2} among representative catalysts summarized from recent publications in 1 M KOH solution.

equivalent-circuit fitting (Fig. S22), reveal that Ru@NiFe PPc exhibits the smallest semicircle radius, indicative of the lowest charge-transfer resistance among all samples (Table S7). The corresponding equivalent circuit used for fitting the Ru@NiFe PPc impedance data is shown in Fig. S23. This improvement is attributed to the excellent electrical conductivity provided by the graphene component and the strong electronic coupling between Ru nanoparticles and the NiFe PPc matrix. In addition, H_2O contact angle measurements demonstrated that Ru@NiFe PPc exhibits superior hydrophilicity (12.3°) compared with NiFe PPc (141°), Ru@G (58.1°), graphene on carbon cloth (G@CC, 141°), and Pt/C (144.1°) (Fig. S24). The superhydrophilic nature of Ru@NiFe PPc is attributed to the oxygen-containing surface groups and enhanced H_2O adsorption capability of Ru nanoparticles formed during electrochemical deposition. Such hydrophilicity facilitates improved electrolyte accessibility, efficient mass transport, increased exposure of active sites, and reduced charge-transfer resistance all of which contribute to enhanced HER kinetics. Catalyst durability was assessed through chronoamperometric measurements and continuous potential cycling tests. As shown in Fig. 3e, Ru@NiFe PPc maintains a stable potential at a current density of 100 mA cm^{-2} for prolonged operation exceeding 1000 h with negligible degradation. In contrast, Ru@G and commercial Pt/C exhibit obvious potential decay under the same conditions. As illustrated in Fig. S25, the polarization curves recorded before and after 3000 CV cycles almost coincide, confirming the robust structural stability and corrosion resistance of the catalyst under alkaline HER conditions. To further verify the structural stability after long-term cycling, a series of post-stability

characterizations were conducted. The TEM images reveal that the overall morphology and structural features of the catalyst remain well preserved after 3000 CV cycles (Fig. S26†). In addition, XPS analysis shows that the binding energies of Ru and Ni exhibit negligible shifts (Fig. S27†), indicating that the electronic structure is largely maintained. The XRD patterns also display nearly identical diffraction peaks for Ru before and after cycling, suggesting the preserved crystalline structure (Fig. S28†). Raman spectra show no noticeable changes, confirming the structural integrity of the catalyst after prolonged electrochemical operation (Fig. S29). ICP-OES analyses reveal negligible changes in the Ru, Fe, and Ni contents, demonstrating the excellent compositional stability of Ru@NiFe PPc (Table S8 and S9). Furthermore, the electrochemically active surface area (ECSA) calculated before and after the cycling test shows negligible variation (Fig. S30 and S31), suggesting that the number of accessible active sites remains largely unchanged after prolonged operation.

Fig. 3f summarizes the comparison of key electrocatalytic parameters—including H_2O contact angle, ECSA, Tafel slope, and overpotential—highlighting the outstanding HER performance of Ru@NiFe PPc. The overpotential values of representative catalysts reported in the literature (Fig. 3g and Table S10) further demonstrate that Ru@NiFe PPc outperforms most state-of-the-art HER catalysts under alkaline conditions at 10 mA cm^{-2}.[19,48–50]

Encouraged by the exceptional HER performance, we next evaluated the practical water-splitting capability of Ru@NiFe PPc in both alkaline two-electrode and anion exchange membrane (AEM) electrolyzer configurations. A two-electrode alkaline electrolyzer was first assembled using Ru@NiFe PPc as the cathode and commercial $NiFeO_x$ as the anode (Fig. S32), with Pt/C and NiFe PPc included as benchmarks. The Ru@NiFe PPc-based device requires a cell voltage that is 1.81 mV lower than Pt/C and 1.92 mV lower than NiFe PPc to reach 100 mA cm^{-2} in 1.0 M KOH, demonstrating its superior catalytic efficiency. To further assess performance under practically relevant conditions, an AEM water electrolyzer was constructed using a simple sandwich-type configuration composed of a current collector, catalyst-coated electrodes, and an AEM without hot-pressing (Fig. 4a and S33). As shown in Fig. 4b, the Ru@NiFe PPc-based AEM electrolyzer exhibits a strong temperature-dependent enhancement (Table S11). Notably, at 80 °C, the device delivers an impressive 2.0 A cm^{-2} at only 2.09 V, surpassing the performance of Pt/C (2.34 V at 2.0 A cm^{-2}) and NiFe PPc (2.67 V at 2.0 A cm^{-2}) (Fig. 4c and S34). Furthermore, long-term chronopotentiometry at 500 mA cm^{-2} demonstrates negligible potential decay over nearly 90 h (Fig. 4d), confirming the remarkable durability of Ru@NiFe PPc for sustained industrial-level hydrogen production.

Beyond conventional H_2O splitting, the intrinsic mixed-valence Ru centers and conductive 2D heterostructure also motivate the use of Ru@NiFe PPc in hybrid electrolysis systems. We therefore integrated Ru@NiFe PPc as the HER cathode with a copper-foam anode to drive the selective electrooxidation of 5-hydroxymethylfurfural (HMF), with Pt/C serving as a control (Fig. 4e). HMF, an abundant biomass-derived platform molecule, can be electrooxidized to 5-hydroxymethyl-2-furancarboxylic acid (HMFCA), a valuable intermediate for furanic polyesters, pharmaceuticals, and fragrances. As shown in Fig. 4f, anodic HMF oxidation significantly lowers the overall operating voltage compared with OER. Remarkably, the bipolar H_2-production system exhibits an onset voltage below 0.1 V and achieves 100 mA cm^{-2} at a cell voltage of only 0.30 V—substantially lower than Pt/C (0.33 V) and drastically reduced compared with conventional alkaline H_2O splitting (1.58 V) (Fig. 4g). These results highlight the exceptional promise of Ru@NiFe PPc as a versatile, energy-efficient catalyst platform for both traditional and hybrid electrochemical H_2 production.

2.3 Theoretical insights into the catalytic mechanism

To elucidate the origin of the superior HER activity of Ru@NiFe PPc@G, we performed density functional theory (DFT) calculations. Based on experimental characterizations, we constructed a slab model featuring small Ru nanoparticles anchored on NiFe PPc *via* Ru–N bonds to mimic Ru@NiFe PPc@G (Fig. S35). To determine the most favorable anchoring configuration of Ru on the NiFe PPc surface, several possible Ru anchoring structures with different Ru–N coordination environments were constructed and fully optimized (Fig. S36). The calculated total energies reveal that one configuration exhibits the lowest energy, indicating that it is thermodynamically the most stable anchoring structure. This optimized Ru–N coordinated configuration was therefore adopted as the representative Ru@NiFe PPc model for subsequent DFT calculations.For comparison, models of pristine NiFe PPc and Ru nanoparticles on graphene (Ru@G) were also built. Charge-density difference analysis reveals substantial electron accumulation at the Ru–N interfaces, confirming strong electronic coupling between Ru nanoparticles and the NiFe PPc framework (Fig. S37). Charge density difference ($\Delta\rho$) analysis reveals that Ru nanoparticles transfer a $\Delta\rho$ of 1.268 e^- to the 2D NiFe PPc/graphene heterostructure in the Ru@NiFe PPc model, whereas Ru nanoparticles transfer a $\Delta\rho$ of only 0.721 e^- to graphene in the Ru@G model (Fig. S38), which is in excellent agreement with the XPS and XAFS results. The alkaline HER pathway involves three elementary steps: H_2O adsorption, $*H_2O$ dissociation, and H_2 desorption (Fig. 5a).

To obtain the most representative theoretical structures and gain deeper insight into the catalytic behavior, additional models were constructed based on different Ru cluster sizes and metal–support environments. Specifically, Ru19 nanoparticles supported on NiFe polyphthalocyanine (Ru19@NiFe PPc), Ru13 nanoparticles supported on Fe phthalocyanine (Ru13@FePc), and Ru13 nanoparticles supported on Ni phthalocyanine (Ru13@NiPc) were also built and fully optimized. Based on these models, the HER reaction pathways were systematically analyzed, and the corresponding water dissociation energy barriers on different catalytic systems were calculated. The resulting comparison of water dissociation barriers for the different catalysts during HER is summarized in Fig. 5b and S39. The calculated H_2O adsorption energy on Ru@NiFe PPc@G is −0.74 eV, significantly more favorable than on Ru@G (−0.59

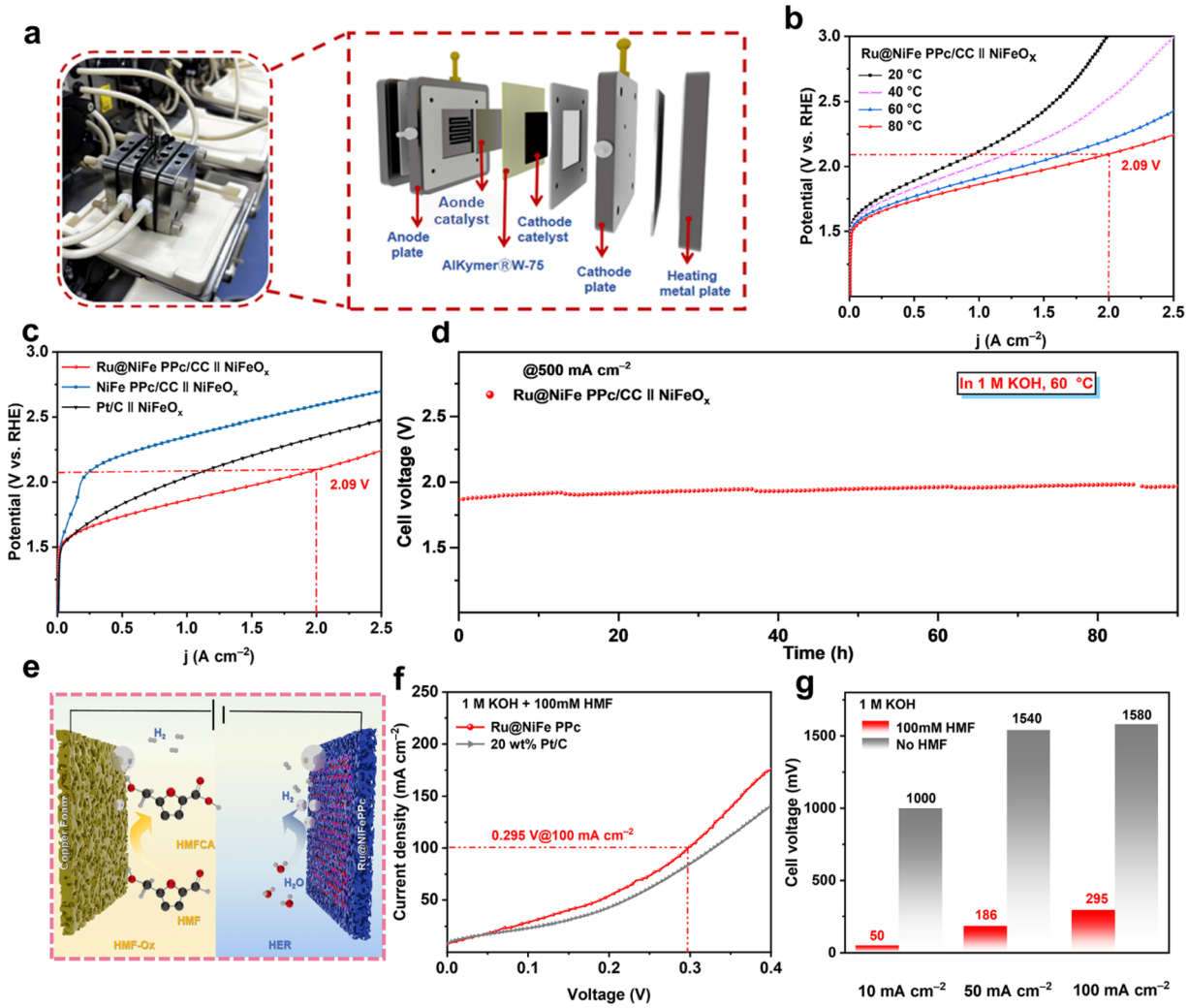

Fig. 4 Characterization of H_2O splitting device at cell level corresponding performance in a bipolar hydrogen production system. (a) The diagram of AEMWE assembly configuration. (b) Polarization curves of Ru@NiFe PPc||$NiFeO_X$ systems in AEMWE at different temperatures. (c) Long-term chronopotentiometry test of the Ru@NiFe PPc||$NiFeO_X$ couple at 500 mA cm^{-2} in the AEMWE system, conducted in 1.0 M KOH at 60 °C. (d) Polarization curves of Ru@NiFe PPc||$NiFeO_X$ systems comparing with NiFe PPc and 20 wt% commercial Pt/C. (e) Schematic representation of the dual-electrode electrolyser, featuring HMF oxidation at low potential on the anode and the hydrogen evolution reaction on the cathode. (f) LSV curves of HMF oxidation in the electrolyser using Cu foam as the anode and Ru@NiFe PPc as the cathode. (g) The cell voltage comparison between normal HER and HFM oxidation system.

eV) and NiFe PPc (0.21 eV). More importantly, the activation barrier for H_2O dissociation drops dramatically to 1.05 eV on Ru@NiFe PPc@G, compared with 1.38 eV on Ru@G and 2.14 eV on NiFe PPc. This facilitation arises from synergistic effects: the partially oxidized Ru^{4+} sites strongly bind H_2O, and form N–H interactions (2.19 Å) from the $*H_2O$ and adjacent N atoms on NiFe PPc framework, elongating the O–H bond to 0.992 Å and thereby weakening it (Fig. 5c and S40). Furthermore, the theoretical prediction of facilitated water activation on Ru@NiFe PPc@G is well supported by *operando* Raman spectroscopy. As shown in Fig. S41, the evolution of interfacial water structures was monitored under increasing overpotentials. For Ru@NiFe PPc, a distinct Raman band corresponding to weakly hydrogen-bonded "free" water (K-H_2O) gradually emerges and intensifies with increasing overpotential, indicating the formation of more weakly bound interfacial water molecules during the HER process. In contrast, such evolution is much less pronounced for the Ru@G and NiFe PPc counterparts. This observation suggests that the Ru@NiFe PPc catalyst more effectively modulates the interfacial water configuration and promotes the generation of free water species under HER conditions. The appearance of these weakly hydrogen-bonded water structures is consistent with the DFT results showing a significantly reduced water dissociation barrier on Ru@NiFe and PPc@G, further confirming that the Ru–N interfacial electronic interaction facilitates water activation and accelerates the alkaline HER kinetics.

To gain insights into the *OH poisoning effect on the Ru nanoparticles, we plotted and compared the charge density difference, the projected density of states (PDOS) of adsorbed

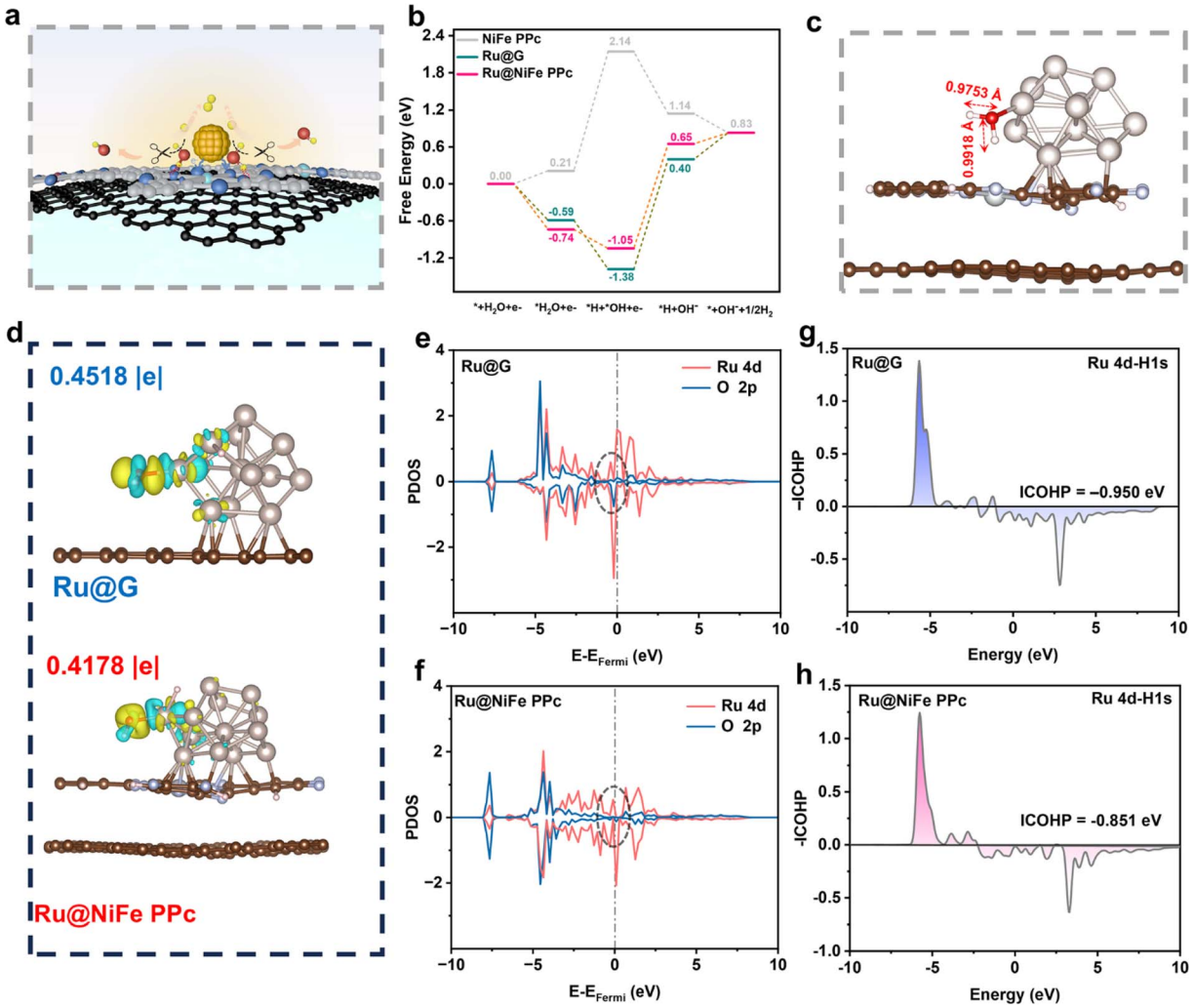

Fig. 5 Schematic illustrating the HER mechanism of Ru@NiFe PPc in alkaline media and the theoretical insights into its improved reaction kinetics. (a) Reaction pathways for HER mechanism on Ru@NiFe PPc. (b) Calculated free energy diagram for hydrogen migration path on Ru@NiFe PPc, Ru@G, and NiFe PPc. (c) Schematic illustration of a H_2O molecule adsorbed on Ru nanoparticles with an elongated hydrogen bond. (d) The Bader charge analysis of the Ru site. The yellow and blue areas represent electron accumulation and electron depletion, respectively, with the isosurface values of 0.005 e/Å^3. The PDOS of *OH on *OH adsorption models for (e) Ru@G and (f) Ru@NiFe PPc. The ICOHP of absorbed H and active Ru site for (g) Ru@G and (h) Ru@NiFe PPc.

*OH for Ru@G and Ru@NiFe PPc. As shown in Fig. 5d, Bader charge analysis shows reduced electron transfer from *OH to Ru in Ru@NiFe PPc@G (0.418 eV) *versus* Ru@G (0.452 eV), indicating that Ru@NiFe PPc possesses a weaker OH binding affinity than Ru@G. PDOS further reveals weaker orbital overlap between O 2p and Ru 4d states in Ru@NiFe PPc@G across the −10 to +10 eV window (Fig. 5e and f),[25,51] consistent with mitigated *OH poisoning (Fig. S42).

As for the adsorbed *H, the free-energy barrier decreases from 0.43 eV on Ru@G to 0.18 eV on Ru@NiFe PPc@G (Fig. 5b). Reasonably, we found that after H_2O dissociation, the generated H species tend to spill over onto the upper surface of the Ru nanoparticles, driven by the strong interfacial interactions at the Ru/NiFe PPc interface (Fig. S43). Bader charge analysis demonstrates that the charge transferred from Ru to *H is 0.256 |e| on the Ru@G model and 0.250 |e| on the Ru@NiFe PPc model (Fig. S44), with the smaller charge transfer indicating weaker H adsorption on Ru@NiFe PPc.[52,53] Crystal orbital Hamiltonian population (COHP) analysis yields a less negative integrated COHP (−0.851 eV) for Ru–H on Ru@NiFe PPc@G than on Ru@G (−0.950 eV) (Fig. 5g and h), confirming optimally weakened H adsorption that favors H_2 desorption.[25,52,54] Collectively, the strong metal–support interaction in Ru@NiFe PPc@G electronically modulates Ru sites to accelerate H_2O dissociation, alleviate *OH poisoning, and optimize H binding for the experimentally observed benchmark alkaline HER performance.

3 Conclusions

In summary, the Ru nanoparticles anchored on two-dimensional metal phthalocyanine/graphene vdW heterostructure (Ru@NiFe PPc) catalyst was constructed for alkaline hydrogen evolution reaction (HER). The graphene/metal-

phthalocyanine polymer two-dimensional vdW heterojunction enhances the catalyst's electrical conductivity and the exposure of active sites. The strong interfacial interaction between the N-rich framework of the modified metal-phthalocyanine polymer and Ru nanoparticles promotes the formation of localized Ru^{4+} species while stabilizing highly active Ru nanoparticles, thereby improving both the HER activity and stability of Ru@NiFe PPc. The resulting Ru@NiFe PPc exhibited the exceptional HER performance in 1 M KOH, achieving a low overpotential of 15 mV at 10 mA cm^{-2}, a small Tafel slope of 39 mV dec^{-1}, and robust stability, outperforming the benchmark 20% Pt/C. Furthermore, the Ru@NiFe PPc based assembled anion-exchange membrane H_2O electrolyzer delivers industrial-scale current density of 2.0 A cm^{-2} at 2.09 V (80 °C), and maintains stable operation at mA cm^{-2} with negligible voltage decay over 90 h. In a hybrid electrolyzer coupling HER with low-potential 5-hydroxymethylfurfural oxidation, the system achieves 100 mA cm^{-2} at a low cell voltage of 0.30 V, dramatically reduces energy consumption for H_2 production coupled with biomass valorization. DFT calculations reveal that the strong metal–support interaction between Ru nanoparticles and NiFe PPc/graphene heterostructure synergistically accelerates H_2O dissociation, alleviates OH poisoning, and optimizes H desorption, enabling benchmark alkaline HER performance. This work pioneers a pyrolysis-free Ru-based vdW heterostructure enabling precise mixed-valence Ru engineering on a conductive phthalocyanine/graphene scaffold, and promises broader advancements in multifunctional electrocatalysis for renewable energy conversion.

Author contributions

Z. X. and G. W. contributed equally to this work. Y. C. and L. L., conceived and designed the experiments, and guided the project. Z. X. and G. W., performed the material synthesis, catalytic performance tests, and structural characterizations. Z. X., G. W., A. Y., S. L., S. X., and Y. Z., participated in the discussion and data analysis. Z. X., G. W., Y. C., and L. L., wrote the manuscript. All authors discussed and commented on the manuscript and approved the submission.

Conflicts of interest

The authors declare no competing financial interest.

Data availability

The data supporting this article have been included as part of the supplementary information (SI). Supplementary information: the experimental section, simulation models, FT-IR spectra, SEM, TEM, HR-TEM images, EDX spectra, XRD patterns, XPS spectra, UV spectra, and ICP-OES details. See DOI: https://doi.org/10.1039/d6sc00386a.

Acknowledgements

The authors acknowledge financial support from the National Natural Science Foundation of China (52403263), Natural Science Foundation of Jiangxi Province (20252BAC200299, 20244BCE52213), and Graduate Students Innovation Special Foundation of Jiangxi Province (YC2025-S227).

Notes and references

1 Q. Sha, S. Wang, L. Yan, Y. Feng, Z. Zhang, S. Li, X. Guo, T. Li, H. Li, Z. Zhuang, D. Zhou, B. Liu and X. Sun, *Nature*, 2025, **639**, 360–367.
2 Y. Zuo, S. Bellani, M. Ferri, G. Saleh, D. V. Shinde, M. I. Zappia, R. Brescia, M. Prato, L. De Trizio, I. Infante, F. Bonaccorso and L. Manna, *Nat. Commun.*, 2023, **14**, 4680.
3 K. Yue, R. Lu, M. Gao, F. Song, Y. Dai, C. Xia, B. Mei, H. Dong, R. Qi, D. Zhang, J. Zhang, Z. Wang, F. Huang, B. Y. Xia and Y. Yan, *Science*, 2025, **388**, 430–436.
4 J. G. Segovia-Hernández, S. Hernández, E. Cossío-Vargas, M. Juarez-García and E. Sánchez-Ramírez, *RSC Sustain.*, 2025, **3**, 134–157.
5 A. Kumar, P. Daw and D. Milstein, *Chem. Rev.*, 2022, **122**, 385–441.
6 T. Zhang, Q. Ye, Z. Han, Q. Liu, Y. Liu, D. Wu and H. J. Fan, *Nat. Commun.*, 2024, **15**, 6508.
7 R. Yao, K. Sun, K. Zhang, Y. Wu, Y. Du, Q. Zhao, G. Liu, C. Chen, Y. Sun and J. Li, *Nat. Commun.*, 2024, **15**, 2218.
8 L. Li, *Nat. Catal.*, 2025, **8**, 856.
9 S. W. Boettcher, *Chem. Rev.*, 2024, **124**, 13095–13098.
10 L. Miao, W. Jia, X. Cao and L. Jiao, *Chem. Soc. Rev.*, 2024, **53**, 2771–2807.
11 M. N. Lakhan, A. Hanan, A. Hussain, I. Ali Soomro, Y. Wang, M. Ahmed, U. Aftab, H. Sun and H. Arandiyan, *Chem. Commun.*, 2024, **60**, 5104–5135.
12 G. Xu, J. Li, Y. Zeng, Z. Shi, W. Qi, K. Li, M. Xiao, C. Liu, W. Xing and J. Zhu, *Energy Environ. Sci.*, 2025, **18**, 6273–6282.
13 K. Deng, X. Liu, P. Liu, X. Lv, W. Tian and J. Ji, *Angew. Chem., Int. Ed.*, 2025, **64**, e202416763.
14 L. Zhang, H. Hu, C. Sun, D. Xiao, H. T. Wang, Y. Xiao, S. Zhao, K. H. Chen, W. X. Lin, Y. C. Shao, X. Wang, C. W. Pao and L. Han, *Nat. Commun.*, 2024, **15**, 7179.
15 W. Li, Z. Ni, O. Akdim, T. Liu, B. Zhu, P. Kuang and J. Yu, *Adv. Mater.*, 2025, **37**, e2503742.
16 A. B. Sorokin, *Chem. Rev.*, 2013, **113**, 8152–8191.
17 Z. Liu, J. Yang, Y. Yan, Y. Feng, M. Wang, X. Wang, G. Chen and J. Zhou, *Adv. Funct. Mater.*, 2025, **35**, 2508638.
18 Y. Zheng, Y. Jiao, Y. Zhu, L. H. Li, Y. Han, Y. Chen, M. Jaroniec and S.-Z. Qiao, *J. Am. Chem. Soc.*, 2016, **138**, 16174–16181.
19 Y. Zhu, L. Li, H. Cheng and J. Ma, *JACS Au*, 2024, **4**, 4639–4654.
20 Y. Li, S. Niu, P. Liu, R. Pan, H. Zhang, N. Ahmad, Y. Shi, X. Liang, M. Cheng, S. Chen, J. Du, M. Hu, D. Wang, W. Chen and Y. Li, *Angew. Chem., Int. Ed.*, 2024, **63**, e202316755.

21 Y. Zhai, L. Cai, Z. Gong, W. Hu and Z. Li, *CrystEngComm*, 2024, **26**, 995–1003.
22 Q. Zhao, Z. Yan, C. Chen and J. Chen, *Chem. Rev.*, 2017, **117**, 10121–10211.
23 Q. P. Ngo, T. T. Nguyen, Q. T. T. Le, J. H. Lee and N. H. Kim, *Adv. Energy Mater.*, 2023, **13**, 2301841.
24 Y. Chen, Y. Liu, L. Li, T. Sakthivel, Z. Guo and Z. Dai, *Adv. Funct. Mater.*, 2024, **34**, 2401452.
25 S. Zhu, Z. Li, L. Hou, M. G. Kim, H. Jang, S. Liu and X. Liu, *Adv. Funct. Mater.*, 2023, **34**, 2314899.
26 Q. Hu, K. Gao, X. Wang, H. Zheng, J. Cao, L. Mi, Q. Huo, H. Yang, J. Liu and C. He, *Nat. Commun.*, 2022, **13**, 3958.
27 Z. Kou, Y. Liu, W. Cui, B. Yang, Z. Li, R. D. Rodriguez, Q. Zhang, C.-L. Dong, X. Sang, L. Lei, T. Zhang and Y. Hou, *Energy Environ. Sci.*, 2024, **17**, 1540–1548.
28 Y. Zang, D. Q. Lu, K. Wang, B. Li, P. Peng, Y. Q. Lan and S. Q. Zang, *Nat. Commun.*, 2023, **14**, 1792.
29 H. Zhong, M. Wang, M. Ghorbani-Asl, J. Zhang, K. H. Ly, Z. Liao, G. Chen, Y. Wei, B. P. Biswal, E. Zschech, I. M. Weidinger, A. V. Krasheninnikov, R. Dong and X. Feng, *J. Am. Chem. Soc.*, 2021, **143**, 19992–20000.
30 P. A. Kempler, R. H. Coridan and L. Luo, *Chem. Rev.*, 2024, **124**, 10964–11007.
31 A. Adalder, K. Mitra, S. Bhowmick and U. K. Ghorai, *Adv. Energy Mater.*, 2025, e05111.
32 J. Zhao, R. Urrego-Ortiz, N. Liao, F. Calle-Vallejo and J. Luo, *Nat. Commun.*, 2024, **15**, 6391.
33 K. Jiang, M. Luo, Z. Liu, M. Peng, D. Chen, Y.-R. Lu, T.-S. Chan, F. M. F. de Groot and Y. Tan, *Nat. Commun.*, 2021, **12**, 1687.
34 F. Abdelghafar, X. Xu, S. P. Jiang and Z. Shao, *Mater. Rep. Energy*, 2022, **2**, 100144.
35 Z. Huang, Y. Wang, J. Xia, S. Hu, N. Chen, T. Ding, C. Zhan, C.-W. Pao, Z. Hu, W.-H. Huang, T. Shi, X. Meng, Y. Xu, L. Cao and X. Huang, *Sci. Adv.*, 2024, **10**, eadq6727.
36 S. Yang, Y. Yu, M. Dou, Z. Zhang, L. Dai and F. Wang, *Angew. Chem., Int. Ed.*, 2019, **58**, 14724–14730.
37 T. S. Nguyen, Y. Hong, N. A. Dogan and C. T. Yavuz, *Chem. Mater.*, 2020, **32**, 5343–5349.
38 J.-C. Xu, S.-M. Xiao, H.-C. Li, Z.-Q. Huang, L.-B. Li and Y.-W. Chen, *Chin. J. Polym. Sci.*, 2025, **43**, 2231–2240.
39 L. Li, X. Tang, S. Huang, C. Lu, D. Lutzenkirchen-Hecht, K. Yuan, X. Zhuang and Y. Chen, *Angew. Chem., Int. Ed.*, 2023, **62**, e202301642.
40 K. Wu, K. Sun, S. Liu, W.-C. Cheong, Z. Chen, C. Zhang, Y. Pan, Y. Cheng, Z. Zhuang, X. Wei, Y. Wang, L. Zheng, Q. Zhang, D. Wang, Q. Peng, C. Chen and Y. Li, *Nano Energy*, 2021, **80**, 105467.
41 X. Tan, H. Li, W. Zhang, K. Jiang, S. Zhai, W. Zhang, N. Chen, H. Li and Z. Li, *Chem Catal.*, 2022, **2**, 816–835.
42 Y. Ding, L. Li, S. Xu, B. Zhou, J. Wang and Y. Chen, *Sci. China Chem.*, 2025, **68**, 1522–1532.
43 V. Ramalingam, P. Varadhan, H.-C. Fu, H. Kim, D. Zhang, S. Chen, L. Song, D. Ma, Y. Wang, H. N. Alshareef and J.-H. He, *Adv. Mater.*, 2019, **31**, 1903841.
44 P. Zhai, M. Xia, Y. Wu, G. Zhang, J. Gao, B. Zhang, S. Cao, Y. Zhang, Z. Li, Z. Fan, C. Wang, X. Zhang, J. T. Miller, L. Sun and J. Hou, *Nat. Commun.*, 2021, **12**, 4587.
45 H. Su, S. Song, Y. Gao, N. Li, Y. Fu, L. Ge, W. Song, J. Liu and T. Ma, *Adv. Funct. Mater.*, 2022, **32**, 2109731.
46 J. Chen, Y. Ha, R. Wang, Y. Liu, H. Xu, B. Shang, R. Wu and H. Pan, *Nano-Micro Lett.*, 2022, **14**, 186.
47 F. Sun, Q. Tang and D.-e. Jiang, *ACS Catal.*, 2022, **12**, 8404–8433.
48 R. A. Marquez, M. Espinosa, E. Kalokowski, Y. J. Son, K. Kawashima, T. V. Le, C. E. Chukwuneke and C. B. Mullins, *ACS Energy Lett.*, 2024, **9**, 547–555.
49 S. Liu, Y. Wei, M. Wang and Y. Shen, *Coord. Chem. Rev.*, 2025, **522**, 216190.
50 R. A. Marquez, J. T. Bender, A. M. Aleman, E. Kalokowski, T. Vy Le, C. L. Williamson, M. L. Frederiksen, K. Kawashima, C. E. Chukwuneke, A. Dolocan, D. J. Milliron, J. Resasco, T. F. Jaramillo and C. Buddie Mullins, *Energy Environ. Sci.*, 2025, **18**, 7170–7187.
51 G. Chen, R. Lu, C. Ma, X. Zhang, Z. Wang, Y. Xiong and Y. Han, *Angew. Chem., Int. Ed.*, 2024, **63**, e202411603.
52 X. Chen, X.-T. Wang, J.-B. Le, S.-M. Li, X. Wang, Y.-J. Zhang, P. Radjenovic, Y. Zhao, Y.-H. Wang, X.-M. Lin, J.-C. Dong and J.-F. Li, *Nat. Commun.*, 2023, **14**, 5289.
53 R. Yao, K. Sun, K. Zhang, Y. Wu, Y. Du, Q. Zhao, G. Liu, C. Chen, Y. Sun and J. Li, *Nat. Commun.*, 2024, **15**, 2218.
54 K. Wu, K. Sun, S. Liu, W.-C. Cheong, Z. Chen, C. Zhang, Y. Pan, Y. Cheng, Z. Zhuang, X. Wei, Y. Wang, L. Zheng, Q. Zhang, D. Wang, Q. Peng, C. Chen and Y. Li, *Nano Energy*, 2021, **80**, 105467.